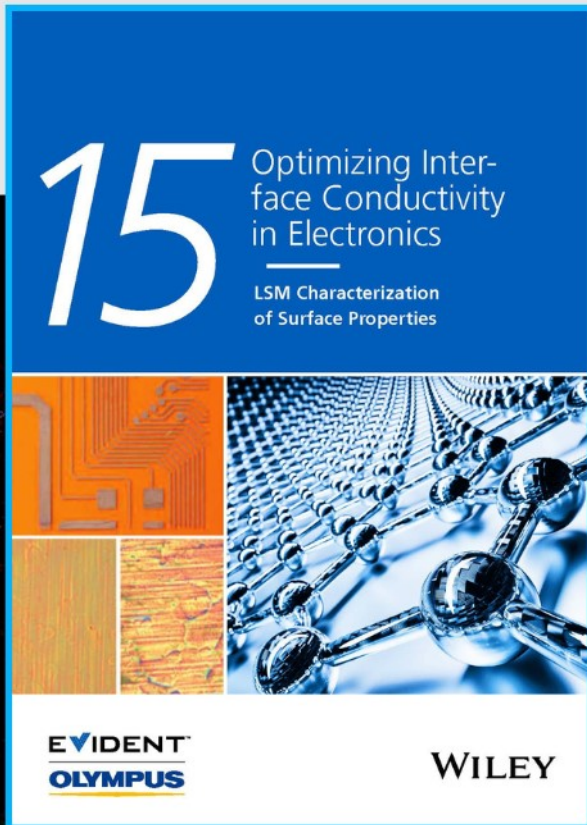




Optimizing Interface Conductivity in Electronics



The latest eBook from
Advanced Optical Metrology.
Download for free.

Surface roughness is a key parameter for judging the performance of a given material's surface quality for its electronic application. A powerful tool to measure surface roughness is 3D laser scanning confocal microscopy (LSM), which will allow you to assess roughness and compare production and finishing methods, and improve these methods based on mathematical models.

Focus on creating high-conductivity electronic devices with minimal power loss using laser scanning microscopy is an effective tool to discern a variety of roughness parameters.

EVIDENT
OLYMPUS

WILEY

Evidence for Glass–glass Interfaces in a Columnar Cu–Zr Nanoglass

Hendrik Voigt,* Aaron Rigoni, Evgeniy Boltynjuk, Mohammed Reda Chellali, Bonnie Tyler, Harald Rösner, Sergiy Divinski, Horst Hahn, and Gerhard Wilde

Comprehensive analyses of the atomic structure using advanced analytical transmission electron microscopy-based methods combined with atom probe tomography confirm the presence of distinct glass–glass interfaces in a columnar Cu–Zr nanoglass synthesized by magnetron sputtering. These analyses provide first-time in-depth characterization of sputtered film nanoglasses and indicate that glass–glass interfaces indeed present an amorphous phase with reduced mass density as compared to the neighboring amorphous regions. Moreover, dedicated analyses of the diffusion kinetics by time-of-flight secondary ion mass spectroscopy (ToF SIMS) prove significantly enhanced diffusivity, suggesting fast transport along the low density glass–glass interfaces. The present results further indicate that sputter deposition is a feasible technique for reliable production of nanoglasses and that some of the concepts proposed for this new class of glassy materials are applicable.

1. Introduction

Nanoglasses have been proposed as a new class of amorphous materials with intrinsically heterogeneous structure and concomitant options for structure-property control that are supposed to go well beyond the limitations known for conventional glasses.^[1] The presence of glass–glass interface regions with an amorphous structure that is distinct from the structure (and properties) of the neighboring regions has been suggested as a hallmark of this new class of amorphous alloys. As a confined glass phase, these interface regions are supposed to allow for variations in mass density, atomic kinetics, elastic moduli, or even magnetic properties from the “parent” glass that significantly exceed property variations that can be adjusted by aging or rejuvenation.^[2–4] These exciting perspectives for such a new class of materials

that have been related to the presence of internal glass-glass interfaces^[5] however are yet to be verified. In addition, a versatile route for reproducible and easily repeatable synthesis of this new class of glasses was lacking until now and has now been established via magnetron sputtering of columnar glassy films with internal glass glass interfaces.^[6–8] The second aspect of the present work is thus related to the analysis of the glass–glass interfaces in magnetron-sputtered thin films to examine if those structures present properties similar to what has been advocated for nano-glasses.

In particular, the glass–glass interfaces in nanoglasses are suggested to have enhanced specific volume as compared to the core regions.^[9,10] Due to the nanometric size of the building blocks of nanoglasses, the total fraction of material within these internal interface regions can be significant, as shown in the past for nanocrystalline materials. The properties of the interface regions can vary drastically from the properties of the core regions, such as the specific volume, or more specifically, the interatomic distance, which affects almost any property of a material.^[11] It goes without saying that the amount and distribution of the excess volume thus presents a potentially powerful parameter for tuning the properties of a nanoglass. In fact, property tuning through controlling the amount of excess volume is very well known for glasses of any binding type and is utilized for many technical applications such as adjusting the refractive index of optical glasses or the electrical resistivity of metallic

H. Voigt, A. Rigoni, H. Rösner, S. Divinski, G. Wilde
University of Münster
Institute of Materials Physics
Wilhelm-Klemm-Str. 10, 48149 Münster, Germany
E-mail: hvoigt@uni-muenster.de

E. Boltynjuk, M. R. Chellali, H. Hahn
Institute of Nanotechnology
Karlsruhe Institute of Technology
Hermann-von-Helmholtz-Platz 1, 76344 Eggenstein-Leopoldshafen,
Germany

B. Tyler
University of Münster
Physikalisches Institut and Center for Soft Nanoscience
Wilhelm-Klemm-Str. 10, 48149 Münster, Germany

H. Hahn
University of Oklahoma
CBME and AME
201 Stephenson Pkwy., Norman OK73019, US

 The ORCID identification number(s) for the author(s) of this article can be found under <https://doi.org/10.1002/adfm.202302386>

© 2023 The Authors. Advanced Functional Materials published by Wiley-VCH GmbH. This is an open access article under the terms of the Creative Commons Attribution-NonCommercial-NoDerivs License, which permits use and distribution in any medium, provided the original work is properly cited, the use is non-commercial and no modifications or adaptations are made.

DOI: 10.1002/adfm.202302386

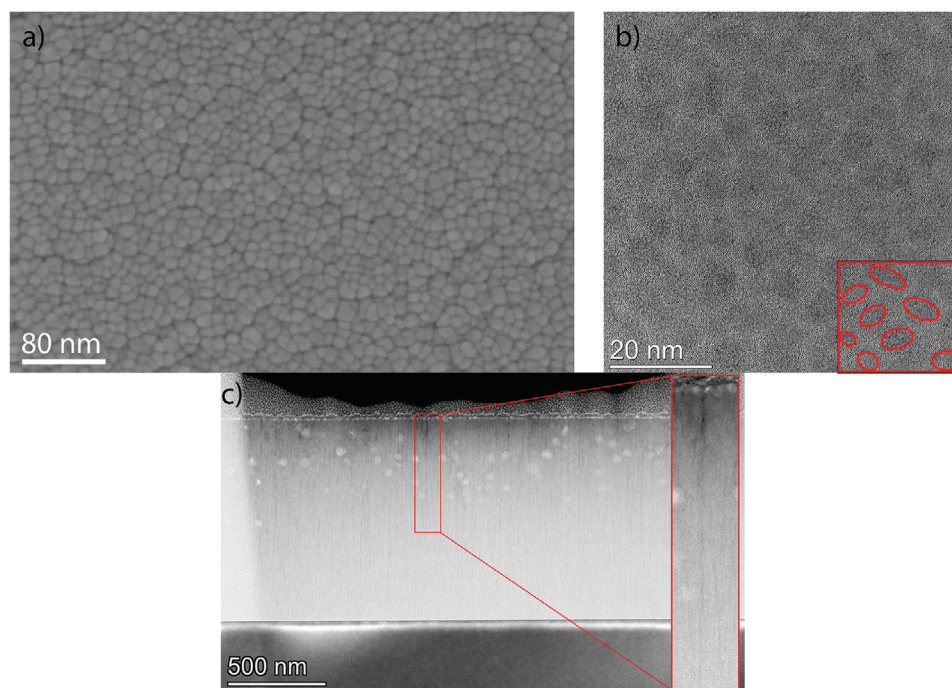


Figure 1. Characteristic micrographs of the sample: a) SEM top view displaying the columnar morphology of the film. b) high-resolution TEM top view image. An inset highlights regions which are separated by glass–glass interfaces c) HAADF-STEM micrograph showing a FIB lamella representing a cross-sectional view of the microstructure. The columnar structure occurs as an alternating contrast of dark channels and brighter matrix. An enlarged image of a channel is shown as inset on the right hand side.

glasses just to mention two examples out of a broad spectrum of applications.^[12,13] Two main issues are new for the concept of nanoglasses: the intrinsic heterogeneity with core regions and spatially confined interface areas with enhanced amount of excess volume and second, the magnitude of excess volume that, according to the hypotheses advanced with the concept of nanoglasses, could be stored within the glass–glass interfaces. It is thus the central purpose of the present work to present structural evidence for core regions separated by glass–glass interfaces in a sputter-deposited nanoglass and to give a first quantitative experimental value for the enhanced excess volume of the glass–glass interface regions by employing a wide range of methods such as nanobeam diffraction,^[14] analytical transmission electron microscopy (TEM), atom probe tomography (APT), and X-ray photoelectron spectroscopy (XPS). Additionally, first diffusion measurements indicate that the glass–glass interfaces could also serve as pathways for faster atomic transport in nanoglasses compared to compositionally equivalent homogeneous amorphous materials. Since the diffusion rates respond exponentially to the changes in the local atomic structures this method is highly sensitive to trace any structural modification.^[15–17]

2. Results and Discussion

2.1. Topological and Chemical Composition

An SEM overview of the structure of the columnar nanoglass thin films is displayed in **Figure 1a**. The corresponding high-resolution TEM micrograph in **Figure 1b** shows a more detailed view of the nanostructured film, revealing that the film is com-

posed of matrix regions separated by channels corresponding to the glass–glass interfaces. An inset highlighting regions separated by glass–glass interfaces is shown in the bottom right. Additionally, the cross-sectional HAADF-STEM image shown in **Figure 1c** gives evidence to the distinct phases of matrix and channel by their dark or bright contrast. The width of the channel regions of about 2 – 4 nm is smaller than the size of the matrix regions. Enlarged views of individual channels are shown as inset of **Figure 1c** and in **Figure 2a**. These images clearly display glass–glass interfaces which have been proposed to exist in nanoglasses prepared by other techniques.^[9] For a schematic representation of the nanoglass structure the reader is referred to [9]. In the cross-sectional TEM images spherical bright spots can be observed which are a result of FIB induced damage. These spots do neither appear in the thicker regions of the TEM lamella nor in the films directly deposited onto TEM grids. For any analysis, these regions have been avoided.

It is important to note that the observed grain-like structure does not originate from open porosity of the sputtered films. Nanoglass samples prepared by IGC on the other hand often suffer from such porosity, thus sputtered films could provide a more reliable alternative production route for nanoglasses.

Core loss EELS analyses revealed a composition of 60 at.% Cu, perfectly matching the nominal composition. However, oxygen was not considered in this particular analysis. To account for the oxygen content, EDX was performed. The results corresponding to the red frame in **Figure 2a** are shown in **Figure 2b** revealing a depletion of Cu inside the channels accompanied by an enrichment of oxygen up to to 35 at.%. A similar oxygen enrichment was reported for homogeneous ZrCuAlNi thin films

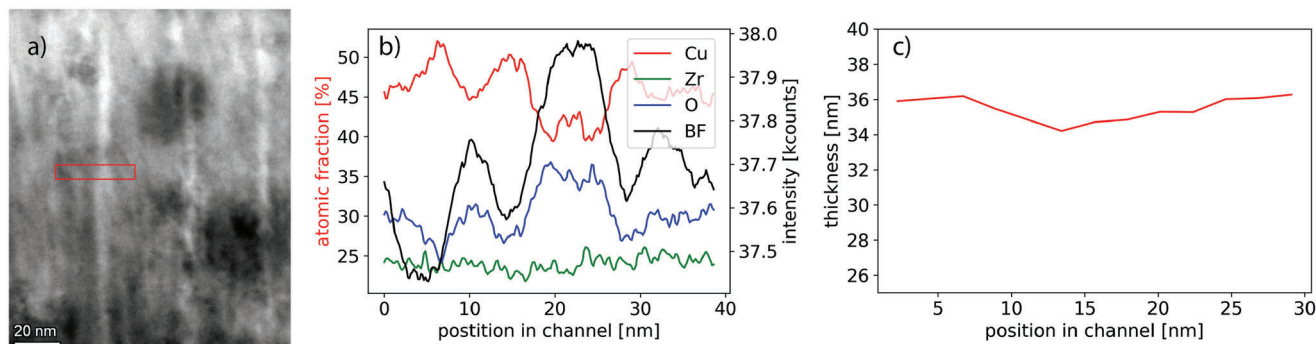


Figure 2. a) Bright-field TEM micrograph of CuZr nanoglass with multiple channels displaying a bright contrast. An EDX linescan corresponding to the red box showing the elemental distribution is displayed in (b). The calculated foil thickness using low-loss EELS is displayed in (c).

after sputtering.^[18] Furthermore, EDX measurements on homogeneous thin film glasses did also show an increased oxygen content of 29 ± 2 at.% homogeneously distributed over an area of $150 \times 150 \text{ nm}^2$ without any preferential clustering.

The origin of the increased oxygen content was analyzed using ToF SIMS measurements, **Figure 3**. To this end, immediately after manufacturing, the samples were kept under a purified ^{18}O atmosphere at room temperature for about 30 min. ToF SIMS depth profiling substantiated that no surplus of ^{18}O with respect to ^{16}O exceeding the natural abundance was developed after this treatment, **Figure 3**. A minor increase of the relative signal of $^{18}\text{O}/^{16}\text{O}$ is detected only at the outer surface, for depths below 10 nm (estimated from the sputtering time). The analysis confirms that the oxygen has entered the material already during synthesis and the oxygen concentration is not strongly affected by short times of exposure to the ambient atmosphere during FIB processing or transportation.

Magnetron sputtering has been shown to be highly sensitive to the residual atmosphere.^[19] For sputtering with a background pressure of $5 \cdot 10^{-8}$ mbar the time to form a single monolayer of oxygen is about 60 s. Additionally, zirconium is a strong getter material that can easily bind oxygen, further increasing the potential oxygen content in CuZr (nano)glasses.

Despite the increased oxygen content in both phases, it was confirmed via NBDP that the structure is still amorphous without

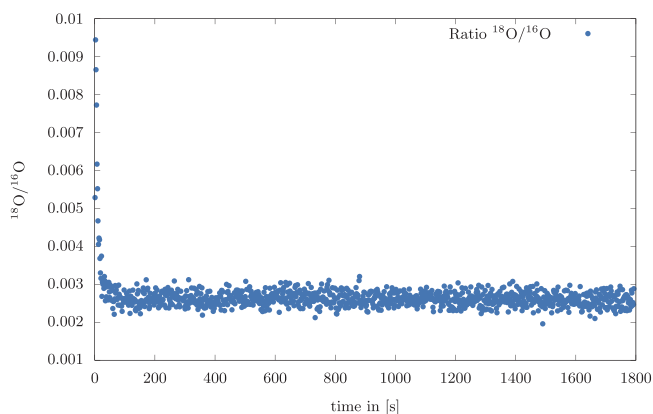


Figure 3. Relative intensity $^{18}\text{O}/^{16}\text{O}$ as measured by ToF SIMS after room temperature exposition to purified ^{18}O atmosphere.

Table 1. Percentage of Cu and Zr atoms identified either in a metallic or and oxide bonding state for both the columnar nanoglass and the homogenous glass.

Sample	Cu		Zr	
	metallic [%]	oxide [%]	metallic [%]	oxide [%]
Columnar NG	79.3 ± 1.1	20.7 ± 1.1	18.7 ± 2.3	81.3 ± 2.3
Homogenous	77.8 ± 1.1	22.2 ± 1.1	31.0 ± 1.9	69.0 ± 1.9

any new phases or precipitates. As a consequence, the oxygen could be treated as a synthesis-inherent alloying element, which is not deteriorating the amorphous state of the nanoglasses.

Additional XPS measurements were performed to explore the binding states of Cu and Zr of the as sputtered samples. The results are taken from a depth interval of 10–226 nm excluding the surface layer and summarized in **Table 1**. It is apparent that both samples show a mixture of metallic and oxide bonding states. For the columnar sample Zr occurs somewhat more frequently in an oxidized state compared with the homogeneous sample. A plausible explanation could be that the oxygen has accumulated in the channels leading to a higher amount of oxidized Zr in these regions. A short paragraph about XPS can be found in the Supporting Information.

The fact that either sample systems contains both bonding types allows still a comparison of their properties as demonstrated e.g., for the introduction of oxygen in a magnetic semiconductor with embedded metallic glass nano-granules.^[20]

APT measurements show a similar enrichment in oxygen inside the channels as observed by EDX (**Figure 4**). Iso-surfaces with increased oxygen content (32%) are highlighted in **Figure 4a**. A slight decrease in sample thickness of about 5% across the channels was recognized using the log-ratio method and is displayed in **Figure 2c**.

2.2. Nanostructure

A series of NBDPs was acquired across a channel with a uniform thickness of about $\approx 22 \text{ nm}$ at the indicated position in **Figure 5a**, which avoids misleading interpretations due to projection artefacts.^[21,22] The corresponding HAADF image from spectrum imaging is shown in **Figure 5b**.

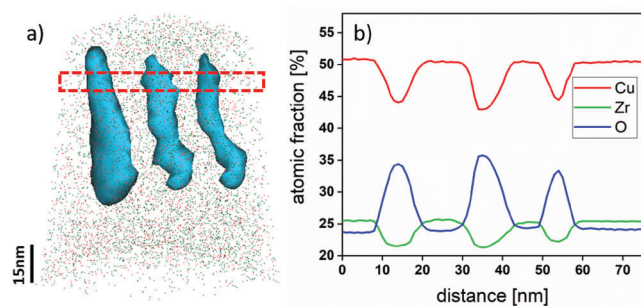


Figure 4. APT analysis of interfaces in columnar CuZr film. a) 3D reconstruction of the columnar structure including the observed channels. A higher O concentration inside the channels is obvious in the elemental map, using the signal of O at 25 at.% (blue) to construct the isosurfaces along channels as indicated in the image. b) 1D composition profile perpendicular to the channels from the region of interest drawn in (a).

In order to enhance the visibility of nanostructural differences between matrix and channels, NMF was performed on the NBDP series. Two NMF factors (Figure 5c,e) display characteristic NBDP and their real space distribution as the corresponding NMF loadings in (Figure 5d,f).

In the two NMF factors, amorphous rings at different k values are visible. The first factor displays a higher contrast at smaller k values, whereas the amorphous ring in the second factor is at higher k values. After azimuthal integration, the amorphous ring of the first factor was determined to be about $k = (3.3 \pm 0.1) \text{ nm}^{-1}$, while the amorphous ring of the second factor was measured at $k = (4.6 \pm 0.1) \text{ nm}^{-1}$. The loading of the first factor shows a stronger contribution of the first factor in the central position of the scanned area, correlating well with the location of the channel. The loading of the second factor is more strongly pronounced at the outer regions of the scanned area, indicating that in the region of the mapped channel NBDP display amorphous rings at smaller k values compared to the NBDP at positions further away from the channel. This observation can be interpreted as an interplay of density change and an increase of the excess volume,^[23] since the k values of the first amorphous ring are smaller inside the channel. This result indicates the existence of two structurally different amorphous phases. The amorphous ring from the first factor was at k values relatively smaller by 28% compared to the k values of the amorphous ring of the second factor. This value can give an upper limit estimation of the enhancement of the excess volume inside the channels. The magnitude of the increase of excess volume seem to be too large on first sight. At this point one should keep two things in mind: First, the NMF analysis yields rather only semi-quantitative results. Second, high values of similar magnitude have been reported earlier for nanoglasses synthesized by compacting amorphous clusters from inert gas condensation.^[9]

Moreover, the NBDP series was further analyzed by a transformation into polar coordinates followed by radial averaging and by subsequently applying Gaussian fit functions $f(x) = \frac{A}{\sigma\sqrt{2\pi}} \exp\left[-\frac{(x-x_0)^2}{2\sigma^2}\right]$ to the first amorphous ring. In this way, height A , centre x_0 and scaling parameter σ corresponding to the FWHM of the fit were determined. The resulting fit parameters are displayed in Figure 5 gh). The channel becomes clearly visible

in the display of both parameters, x_0 and σ . Inside the channel the k values of the first amorphous ring are smaller and the FWHM values are larger, providing an independent confirmation of the NMF. The first amorphous ring was determined to have slightly higher k values for the matrix region as compared to the value identified by the NMF analysis. Averaging the first and last three rows of the fitting parameter center yields a value of $k = (4.42 \pm 0.12) \text{ nm}^{-1}$ whereas averaging the three rows in the center, most likely corresponding to the channel position, yields a value of $k = (3.91 \pm 0.22) \text{ nm}^{-1}$. This more quantitative analysis yields a k value shift of 12% inside the channel regions.

The extraction of excess volume from this k -value shift is now described in more detail. Considering that density changes were due to a compositional changes in Cu and Zr only, a density change of maximally 2% is expected.^[24] However, oxygen has to be taken into account. Using the individual densities of the constituents with $\rho(\text{Cu}) = 8.96 \text{ gcm}^{-3}$, $\rho(\text{Zr}) = 6.50 \text{ gcm}^{-3}$ and $\rho(\text{O}) = 1.14 \text{ gcm}^{-3}$, the densities of matrix and channel were calculated to be $\rho(\text{matrix}) = (5.89 \pm 0.08) \text{ gcm}^{-3}$ and $\rho(\text{channel}) = (5.61 \pm 0.08) \text{ gcm}^{-3}$, respectively. Under the assumption that the density difference between matrix and channel was of purely compositional origin, a value of 5% would be obtained. Estimating now the excess volume from the shift in k values using the approach by Ma et al.^[25] with $k_1 v_a^{0.433 \pm 0.007} = 9.3 \pm 0.2$, where the atomic volume v_a or density is correlated with the first peak in the diffraction pattern k_1 , yields finally a value of about $10 \pm 6\%$ for the excess volume. It is emphasized that the calculation of the excess volume is afflicted with a large uncertainty due to the variance in the shift of the k value. Yet, an increase of the magnitude observed in this study is remarkable and supports the significant structural differences between matrix and channels. More information regarding the calculation can be found in the supplementary. While this value sounds quite large, it is worth mentioning that such values and even higher ones have been reported for the excess volume in shear bands of metallic glasses.^[26] Thus, the observed changes are well within the expected range. Simulations on CuZr nanoglasses yielded an increase of the excess volume by 4%^[27] while simulations on CuTi nanoglasses suggested an increase by about 10%.^[1]

Naturally, such a large increase of the excess volume needs to be accompanied by significant structural modifications. While a typical magnitude for the change of the excess volume of a metallic glass during aging or rejuvenation is confined to about 2% at maximum, nanoglasses display an increase that is up to five times larger. Therefore, a mere modification of the local motifs of the glass (often referred to as short range order or medium range order) is unlikely to suffice for accommodating such pronounced changes in the excess volume. A possible explanation for the magnitudes of excess volume changes observed for nanoglasses might lie in a change of the bonding state, with a more directional bonding contribution leading to local structures that are at the same time less densely packed but mechanically still sufficiently (or even more) stable.

2.3. Diffusion

The concentration profiles measured for Ni diffusion in columnar and homogeneous CuZr films are shown in **Figure 6** in

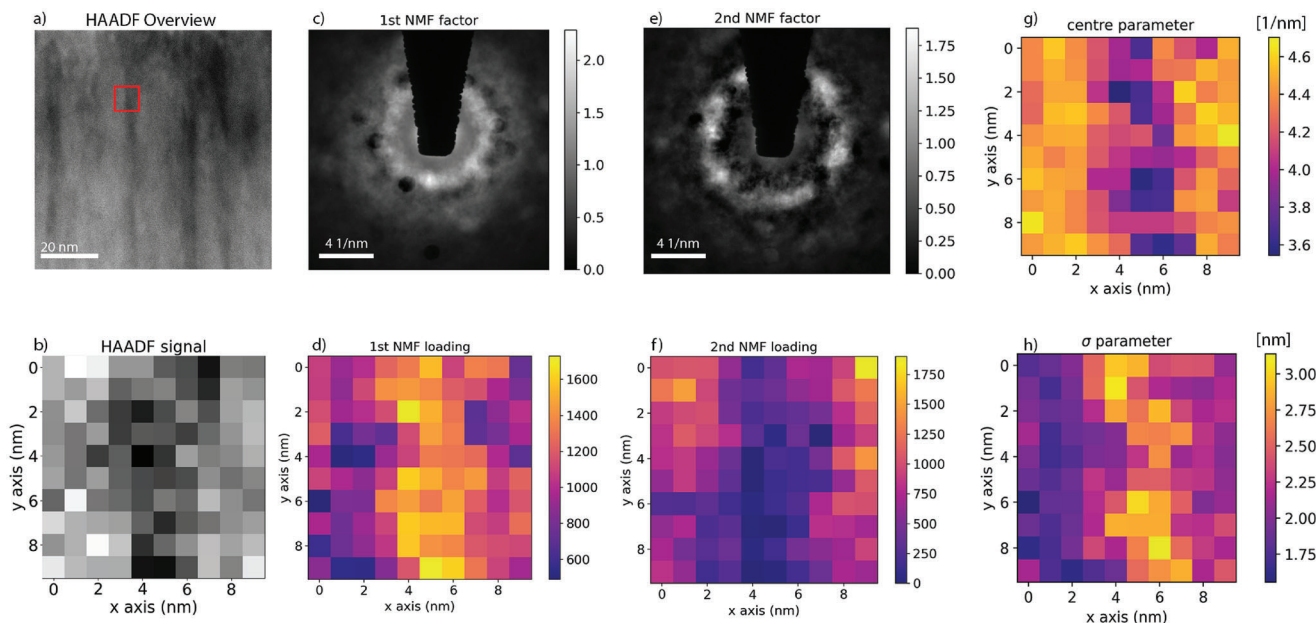


Figure 5. An overview of the sample with an indication of the region used for the NBDP acquisition is shown in (a) while the HAADF spectrum image is displayed in (b). First two factors and factor loadings of NMF analysis in (c–f). Fitting parameters of a Gaussian to the Intensity of the radially averaged NBDP are shown in (g) and (h).

comparison to the corresponding initial (as-prepared) states. Diffusion-induced profile broadening is clearly observed. During ToF SIMS profiling, the samples were sputtered until the Si signal appeared, which allowed an exact depth quantification from the known sputtering time and the film thickness. In Figure 6, the profiles recorded from the external surface to the mid-plane Ni layer are shown (inverted with respect to the depth scale for a clear visualization).

Assuming a thin film solution,^[28] the concentration, $C(x)$, of the tracer element can be approximated by a Gaussian function,

$$C(x) = \frac{C_0}{\sqrt{\pi Dt}} \cdot \exp\left(-\frac{x^2}{4Dt}\right) \quad (1)$$

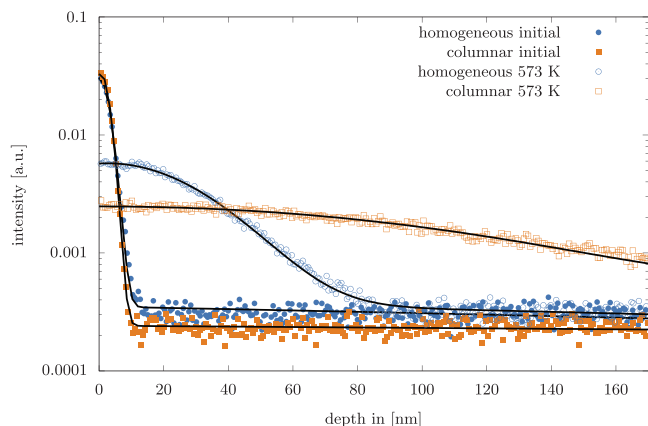


Figure 6. Penetration profiles determined for Ni diffusion in homogeneous (squares) and columnar (circles) CuZr at 573 K (filled symbols) with respect to those in the initial (as-deposited) states (open symbols).

where C_0 is the initial tracer amount, x the depth, t the annealing time and D the diffusion coefficient. This solution was found to provide a satisfactory agreement for diffusion in homogeneous films.

For the annealed columnar samples, the tracer atoms were found to diffuse through the whole sample. Thus the basic solution for infinite systems, Equation 1, cannot be applied anymore. In that case a solution for finite systems was used to describe the measured diffusion profiles mathematically,^[29]

$$C(x) = \frac{1}{2} C_0 \cdot \sum_{n=-\infty}^{\infty} \left\{ \operatorname{erf}\left(\frac{h + 2nl - x}{2\sqrt{Dt}}\right) + \operatorname{erf}\left(\frac{h - 2nl + x}{2\sqrt{Dt}}\right) \right\} \quad (2)$$

where l is the thickness of the sample and h is a factor for considering the shift (used as a fitting parameter).

The obtained data (Figure 6) confirm significantly faster diffusion of Ni in the columnar sample with $D_{col} = (5.38^{+4.53}) \cdot 10^{-20} \text{ m}^2 \text{ s}^{-1}$ in comparison to its homogeneous amorphous counterpart with $D_{hom} = (5.33^{+1.49}) \cdot 10^{-21} \text{ m}^2 \text{ s}^{-1}$ at the temperature of 573 K. Note that D_{hom} in the present CuZr glass turned out to be similar to the value of Ni diffusion in $\text{Zr}_{46.75}\text{Ti}_{8.25}\text{Cu}_{7.5}\text{Ni}_{10}\text{Be}_{27.5}$ bulk metallic glass measured by Knorr et al.,^[30] while on the contrary, the Ni diffusion rate in the columnar nanoglass is by an order of magnitude higher.

3. Conclusion

This work presents a comprehensive analysis of glass–glass interfaces in sputtered thin film columnar nanoglasses of $\text{Cu}_{60}\text{Zr}_{40}$ revealing for the first time clear experimental evidence for their

existence. Thereby, this work verifies unambiguously and for the first time that sputtered columnar glasses bear the characteristics of true nanoglasses. Given the versatility of the sputtering method for nanoglass synthesis, as compared to alternative methods that have been reported so far, this result is of high importance also for a broader range of compositions and applications. The dedicated structural analyses revealed channels with widths ranging on average between 2 – 4 nm. These channels exhibit a different elemental composition compared to the surrounding matrix. A shift to smaller k values was observed for the first amorphous peak inside the channels, which leads to the conclusion that the excess volume inside the channels increased by about $10 \pm 6\%$. This large increase is specific for nanoglasses and has not been reported for bulk metallic glasses. Yet, it should be noted that for another situation where confinement is also playing a role, i.e., for shear bands in plastically deformed metallic glasses an increase of the excess volume up to 11% ^[26,31,32] has also been reported. In these materials such changes of the amorphous structure are commonly accompanied by a change in diffusivity. This observation is further strengthening the hypothesis of tunable glasses through the introduction of glass–glass interfaces.

The increase in diffusivity by one order of magnitude in the nanoglass compared to the homogeneous glass confirms the unique structure of the latter, even though these measurements are macroscopically averaged and cannot reveal the location of fast transport pathways. As a working hypothesis, we suggest that the increased excess volume attributed to the channels is the major reason for the diffusivity increase. It should be recalled that measuring an increased diffusivity due to porosity was excluded through the ^{18}O ToF SIMS measurements.

Perspectively, the present analyses of the atomic structure and kinetics of a sputtered nanoglass confirm early conjectures on this new class of glasses concerning the reduced mass density of glass–glass interfaces and an increased atomic mobility. It thus seems safe to state that sputtering, as a versatile and available method is capable for synthesizing nanoglasses, which opens up new opportunities for changes in composition or for applications. At the same time, interesting questions concerning the local accommodation of the observed large changes of the excess volume and of possible associated changes of e.g., electronic properties are still open. Here, the possibility to synthesize thin films by sputtering presents a new window of opportunity to tackle these open questions.

4. Experimental Section

Thin Films Preparation: Nanoglasses had been synthesized by different methods. The two most prominent methods had been inert gas condensation (IGC) for the production of bulk samples and magnetron sputtering for the synthesis of thin films.^[9] Yet, for the latter, the presence of internal interfaces that qualified those materials as nanoglasses yet required verification. An important aspect for the production of thin film nanoglasses via magnetron sputtering was carefully controlling the sputter parameters such as pressure and gas flow. An adequate choice of these parameters allows for the preparation of nanoglasses with a columnar nanostructure.^[7,9] The investigated samples were grouped as follows: i) samples for structural characterization and ii) samples for the diffusion measurements.

Samples for structural characterization were synthesized from an alloy target of nominal composition of $\text{Cu}_{60}\text{Zr}_{40}$ (in at.%) using Radio Frequency (RF) magnetron sputtering. Sputtering was performed at a power of 100 W, a fixed distance between the substrate and a target diameter of 100 mm, a target tilt angle of 20 degrees and a substrate temperature of 293 K. The background pressure prior to deposition was less than $5 \cdot 10^{-8}$ mbar. The working pressure and flow rate of Ar were kept constant at $8 \cdot 10^{-3}$ mbar and 100 sccm, respectively. Thin films were deposited continuously on Si (100) wafers with a native oxide layer rotating at a velocity of 10 rpm. Additional films with a thickness of 15 nm were deposited directly on Mo TEM-grids with holey carbon film coated with a 2 nm thin carbon layer. For the measurements of Ni diffusion in the $\text{Cu}_{60}\text{Zr}_{40}$ columnar and homogeneous states, thin films were prepared using RF magnetron sputtering with parameters of the chamber as described above. For columnar films, the working pressure and flow rate of Ar were kept constant at $8 \cdot 10^{-3}$ mbar and 100 sccm, respectively. For homogeneous films the working pressure and flow rate of Ar were kept constant at $2.8 \cdot 10^{-3}$ mbar and 40 sccm, respectively. A Ni layer was deposited near the mid-plane of the samples by co-sputtering from another magnetron gun equipped with a target of pure Ni (i.e., sputtering of CuZr films was not interrupted during the entire process of the films synthesis). The shutter for the magnetron gun containing the Ni-target was briefly opened to sputter a 0.5 nm thin Ni layer. This procedure allowed for the distribution of tracer atoms in a 1.5 nm thick layer of the CuZr matrix to avoid discrete interfaces and to reduce the possibility of interfacial contamination.^[33] Sputtering times were chosen to reach a final thickness of about 400 nm. The film thickness was measured with a Veeco Dektak 6M Stylus Profiler and by scanning electron microscopy (SEM LEO 1530, Carl Zeiss AG). Columnar and homogeneous specimens were annealed under vacuum, $<5 \cdot 10^{-8}$ mbar, at a temperature of 573 K for 1003 min. The temperature during the annealing was kept constant in a range of 2 K using a Chromel-Alumel thermocouple to continuously monitor the temperature. Post annealing the amorphous structure was monitored by D8 Discover powder diffractometer.

APT: 3D Atom Probe Tomography (APT) was performed on sharp tip shape samples, prepared using a Zeiss Auriga 60 FIB system. Prior to the lift-out, a platinum protective layer (150 nm in thickness) was deposited over the area of interest to protect the APT sample from the gallium (Ga) ion beam milling damage. To produce the required atom probe specimen geometry, annular milling was used to create a needle-shaped morphology with a tip diameter smaller than 100 nm. The APT measurements were carried out using a Cameca-LEAP 4000X HR instrument in laser pulse mode (wavelength 355 nm, pulse frequency 100 kHz, pulse energy 30 pJ, evaporation rate 0.50%) at 50 K. Data processing was realized with the CAMECA integrated visualization and analysis software (IVAS-version 3.6.1), incorporating standard reconstruction algorithms enabling extraction of the 3D chemical distribution of the analyzed nanosized volume.

TEM Measurements: Electron transparent TEM lamellae revealing cross-sectional views were prepared using a ZEISS Crossbeam 340 FIB with ion beam energies of 35 keV and were finally polished at a low ion energy of 5 keV. Prior to the lift-out, a platinum protective layer was deposited over the area of interest to protect the samples from the milling damage by the Ga ion beam.

The samples were cleaned for two minutes before the TEM measurements using a Fishione Plasma cleaner to avoid contamination. All TEM measurements were performed at 300 kV in a FEI Titan Themis 60–300 (Thermo Fisher Scientific) transmission electron microscope (TEM) equipped with an image C_s corrector and a monochromator using an extraction voltage of 3.45 kV for the X-FEG. Analytical TEM was performed using a quadrupole energy-dispersive X-ray system (Super-X EDX detector), a high-angle annular dark-field (HAADF) detector (Fischione Model 3000), a fast CMOS camera (Ceta, 4k · 4k) and a high-resolution electron energy loss (EEL) spectrometer (Quantum 965 Gatan Imaging Filter). The foil thickness of the TEM lamellae was determined by the log-ratio method using the low-loss part of the electron energy loss (EEL) spectrum.^[34] For the determination of the composition, core loss EELS was employed using the $\text{Cu L}_{2,3}$ (950, 930 eV) and $\text{Zr L}_{2,3}$ (2307, 2222 eV) edges.

Nanobeam diffraction patterns with parallel illumination were acquired over different regions of interest using drift-corrected spectrum imaging

Received: March 1, 2023

Revised: June 5, 2023

Published online:

with a pixel spacing of 1 nm to avoid oversampling, while the probe size was fixed at 1 nm (FWHM).^[35] For this purpose the μ -probe STEM mode was used with a C2 aperture of 10 μ m. The actual probe size was directly measured on the Ceta camera and determined using a custom-made DM plugin by D. Mitchell.^[36] A beam current of 15 pA measured on the fluorescent screen with a nominal spot size eight was used for the NBDPs measurements. The exposure time was set to 4 s with a camera length of 100 mm to ensure a good signal-to-noise ratio. The NBDPs were acquired on a US 2000 Gatan CCD camera at binning 4; that is, 512 \times 512 pixels.

A non-negative matrix factorization (NMF) was applied to the stacks of NBDPs using the python package hyperspy.^[37] NMF decomposes a data set into two positive matrices: for this dataset into representative NBDP (NMF factor) and their spatial distribution maps (NMF factor loading).^[38] A more detailed description of the method is given in the Supporting Information.

Diffusion by ToF SIMS: Diffusion experiments were performed using a highly enriched ¹⁸O isotope and Ni with a natural mixture of stable isotopes. For the ¹⁸O diffusion measurements, a Cu₆₀Zr₄₀ columnar thin film deposited on Si substrate was transferred from the sputtering chamber to the loadlock. After disconnecting the loadlock from the pumping system it was filled with ¹⁸O to a pressure of about 5 mbar and kept for about 30 min. Subsequently, the loadlock was vented and the sample was analyzed using Time-of-Flight Secondary Ion Mass Spectrometry (ToF SIMS), see below.

The concentration-depth profiles of ¹⁸O and natural Ni (mainly of the ⁵⁸Ni isotope) were determined using ToF SIMS with a custom-built instrument, which was equivalent to the IONTOF M6 commercial version. The ToF SIMS was operated at a pressure of <10⁻⁸ mbar. Depth profiles were measured in a dual-beam mode, using a 30 keV Bi³⁺ primary ion source with a pulsed current of 0.02 pA for analysis and a 1 keV Ar source with a current of 200 nA for sputtering. Analysis was conducted over 100 \times 100 μ m² areas and sputtering was conducted over 500 \times 500 μ m² areas. The sputtering depth was determined by means of confocal interferometry and the depth scale was established assuming a constant sputtering rate. The stability of the ion current was permanently controlled during acquisition.

Supporting Information

Supporting Information is available from the Wiley Online Library or from the author.

Acknowledgements

Financial support from the German Science Foundation (DFG - project number WI-1899/42-1 and HA-1344/46-1) was acknowledged. The DFG was further acknowledged for funding our TEM equipment via the Major Research Instrumentation Program under INST 211/719-1 FUGG. The authors would like to thank the Karlsruhe Nano Micro Facility (KNMF) at Karlsruhe Institute of Technology (KIT) for the use of facilities.

Open access funding enabled and organized by Projekt DEAL.

Conflict of Interest

The authors declare no conflict of interest.

Data Availability Statement

The data that support the findings of this study are available from the corresponding author upon reasonable request.

Keywords

diffraction, diffusion, electron microscopy, glass-glass interfaces, nanoglass, sputtering, ToF SIMS

- [1] H. Gleiter, *Acta Mater.* **2008**, *56*, 5875.
- [2] W. Arnold, R. Birringer, C. Braun, H. Gleiter, H. Hahn, S. Nandam, S. Singh, *Trans. Indian Inst. Metals* **2020**, *73*, 1363.
- [3] A. Stoesser, M. Ghafari, A. Kilmametov, H. Gleiter, Y. Sakurai, M. Itou, S. Kohara, H. Hahn, S. Kamali, *J. Appl. Phys.* **2014**, *116*, 134305.
- [4] S. Nandam, Y. Ivanisenko, R. Schwaiger, Z. Śniadecki, X. Mu, D. Wang, R. Chellali, T. Boll, A. Kilmametov, T. Bergfeldt, H. Gleiter, H. Hahn, *Acta Mater.* **2017**, *136*, 181.
- [5] O. Franke, D. Leisen, H. Gleiter, H. Hahn, *J. Mater. Res.* **2014**, *29*, 1210.
- [6] N. Chen, R. Frank, D. V. Louzguine-Luzgin, P. Sharma, J. Q. Wang, G. Q. Xie, Y. Ishikawa, N. Hatakeyama, Y. C. Lin, M. Esashi, Y. Yamamoto, A. Inoue, *Acta Mater.* **2011**, *59*, 6433.
- [7] Z. Śniadecki, D. Wang, Y. Ivanisenko, V. Chakravadhanula, C. Kübel, H. Hahn, H. Gleiter, *Mater. Charact.* **2016**, *113*, 26.
- [8] W. Yao, Q. Cao, S. Liu, X. Wang, H. Fecht, A. Caron, D. Zhang, J. Jiang, *Acta Mater.* **2020**, *194*, 13.
- [9] Y. Ivanisenko, C. Kübel, S. Nandam, C. Wang, X. Mu, O. Adjaoud, K. Albe, H. Hahn, *Adv. Eng. Mater.* **2018**, *20*, 1.
- [10] T. Li, K. Ma, G. Zheng, *J. Mater. Res.* **2021**, *36*, 4951.
- [11] N. Ramesh, P. Davis, J. Zielinski, R. Danner, J. Duda, *J. Polym. Sci., Part B: Polym. Phys.* **2011**, *49*, 1629.
- [12] Y. Huang, H. Fan, S. Guan, Z. Ning, F. Cao, D. Daisenber, J. Sun, *J. Alloys Compd.* **2019**, *789*, 704.
- [13] Z. Zhu, E. Ma, J. Xu, *Intermetallics* **2014**, *46*, 164.
- [14] T. Pekin, J. Ding, C. Gammer, B. Ozdol, C. Ophus, M. Asta, R. Ritchie, A. Minor, *Nat. Commun.* **2019**, *10*, 1.
- [15] A. Paul, T. Laurila, V. Vuorinen, S. Divinski, *Thermodynamics, Diffusion and the Kirkendall Effect in Solids*, Springer, Int. Publ. Switzerland, **2014**, <https://link.springer.com/book/10.1007/978-3-319-07461-0>.
- [16] J. Bokeloh, S. Divinski, G. Reglitz, G. Wilde, *Phys. Rev. Lett.* **2011**, *107*, 1.
- [17] A. Hassanpour, M. Vaidya, S. Divinski, G. Wilde, *Acta Mater.* **2021**, *209*.
- [18] N. Bönninghoff, W. Diyatmika, J. Chu, S. Mráz, J. Schneider, C. Lin, F. Eriksson, G. Greczynski, *Surf. Coat. Technol.* **2021**, *412*, 3.
- [19] P. Pokorný, J. Musil, P. Fitl, M. Novotný, J. Lančok, J. Bulíř, *Plasma Processes Polym.* **2015**, *12*, 416.
- [20] N. Chen, H. Li, A. Hirata, Z. Luo, Z. Wang, W. Liu, B. Cui, T. Hitosugi, L. Gu, X. Zhang, X. Zhang, C. Song, X. Wang, L. Zhang, J. Cao, K. Ohmura, S. V. Ketov, K. Yao, M. Chen, D. V. Louzguine-Luzgin, *Mater. Des.* **2017**, *132*, 208.
- [21] S. Im, Z. Chen, J. Johnson, P. Zhao, G. Yoo, E. Park, Y. Wang, D. Muller, J. Hwang, *Ultramicroscopy* **2018**, *195*, 189.
- [22] J. Rys, L. Valdevit, T. Schaedler, A. Jacobsen, W. Carter, J. Greer, *Adv. Eng. Mater.* **2014**, *16*, 889.
- [23] Y. Deng, L. He, Q. Zhang, H. Zhang, H. Ye, *Ultramicroscopy* **2004**, *98*, 201.
- [24] K. Park, J. Jang, M. Wakeda, Y. Shibutani, J. Lee, *Scr. Mater.* **2007**, *57*, 805.
- [25] D. Ma, A. Stoica, X. Wang, *Nat. Mater.* **2009**, *8*, 30.
- [26] D. Klaumünzer, A. Lazarev, R. Maaß, F. Dalla Torre, A. Vinogradov, J. Löffler, *Phys. Rev. Lett.* **2011**, *107*, 185502.
- [27] K. Zheng, S. Yuan, H. Hahn, P. Branicio, *Sci. Rep.* **2021**, *11*, 1.

- [28] H. Mehrer, *Diffusion in solids: fundamentals, methods, materials, diffusion-controlled processes*, vol. 155, Springer Science & Business Media, Berlin, Germany **2007**.
- [29] J. Crank, *The mathematics of diffusion*, Oxford University Press, Oxford **1979**.
- [30] K. Knorr, M. Macht, K. Freitag, H. Mehrer, *J. Non-Cryst. Solids* **1999**, 250, 669.
- [31] P. Donovan, W. Stobbs, *Acta Metall.* **1981**, 29, 1419.
- [32] H. Rösner, M. Peterlechner, C. Kübel, V. Schmidt, G. Wilde, *Ultramicroscopy* **2014**, 142, 1.
- [33] H. Hahn, R. Averback, *Phys. Rev. B* **1988**, 37, 6533.
- [34] T. Malis, S. C. Cheng, R. F. Egerton, *J. Electron Microsc. Tech.* **1988**, 8, 193.
- [35] J. Tao, D. Niebieskikwiat, M. Varela, W. Luo, M. Schofield, Y. Zhu, M. Salamon, J. Zuo, S. Pantelides, S. Pennycook, *Phys. Rev. Lett.* **2009**, 103, 097202.
- [36] D. Mitchell, B. Schaffer, *Ultramicroscopy* **2005**, 103, 319.
- [37] hyperspy/hyperspy: Release v1.7.1, **2022**, <https://doi.org/10.5281/zenodo.6659919>.
- [38] P. Lucas, G. Burdet, M. Cantoni, C. Hébert, *Micron* **2013**, 52-53, 49.